HiSST: 3rd International Conference on
High-Speed Vehicle Science Technology
14 -19 April 2024, Busan, Korea

A boundary adaptive sharpening topology optimization method for high Reynolds number flow in regenerative cooling structures

Xinlei Li, Kun Wu[1], Xuejun Fan

Abstract

For propulsion systems of air-breathing hypersonic vehicles, an efficient thermal protection system (TPS) is of great significance to ensure the safety of the vehicles. To enhance the heat transfer performance of regenerative cooling system, a fluid-thermal coupled topology optimization (TO) method for high Reynolds number flow is developed. Based on classical density-based topology optimization model, a modified Brinkman-Forchheimer equation for the high Reynolds number flow in porous media is employed, which adaptively forms a boundary sharpening resistance in the optimized channel's solid areas. The n-Decane with variable thermophysical and transport properties is worked as the coolant. Then, the topology optimization is conducted in a continuous adjoint framework constructed in OpenFOAM, and a series of optimization cases with different power dissipation constraints are obtained. Conjugate heat transfer (CHT) simulation is further conducted for both conventional straight channel (SC) and topology optimized channel (TO). It is found that the heat transfer performance of channel TO is significantly enhanced compared to channel SC, and it also brings lower pressure drop and better overall performance.

Keywords: *Regenerative cooling; Topology optimization; High Reynolds number; Variable thermophysical properties; Heat transfer performance*

1. Introduction

Regenerative cooling is one of the most representative forms of scramjet's thermal protection system (TPS) and has been demonstrated on flight test of X-51A [1]. However, the conventional regenerative cooling system has encountered the issue of inadequate cooling capacity as the flight Mach number increases. Consequently, various optimization methodologies for regenerative cooling structures are developed in recent year [2-6]. Among these methodologies, the topology optimization (TO), which possesses the maximum degrees of freedom theoretically, is regarded as one of the most promising tools [7].

In the field of fluid mechanics, researches on topology optimization have been emerged since its first application by Borrvall and Petersson [8], who first researched the topology optimization of fluids in Stokes flow. Gersborg-Hansen et al. [9] extended the method to Navier-Stokes equation by adding an inertial term, then topology optimization designs are conducted for an incompressible laminar flow problem in porous media. It was found that when the Reynolds number increases, the effect of the inertia term will evidently change the topology configurations. Since then, the topology optimization model of turbulent flow has been developed rapidly. Othmer et al. [10] derived the continuous adjoint equation and sensitivity with the hypothesis of "frozen turbulence", and implemented the algorithm based on the finite volume method framework on OpenFOAM. Yoon [11] developed a topology optimization model for turbulent flow based on Spalart-Allmaras (S-A) equation, in which the interpolation functions are added into two transport equations and the wall's function equation. The optimized designs based on laminar and turbulent flow models were further compared, and it concluded that the optimized designs for laminar flow are not effective in turbulent flow cases. Dilgen et al. [12] conducted topology optimization designs for turbulent flow and heat transfer problem on full 3D design domain, the penalized SST k-ω turbulence model is firstly applied and verified to be effective.

[1] *Institute of Mechanics, Chinese Academy of Sciences, Beijing 100190, China. wukun@imech.ac.cn*

In spite of the fact that the topology optimization has been preliminarily applied in the thermal designs of electronic devices or in other energy engineering fields, there are few relevant researches on topology optimization for engine's regeneration cooling structures. In the published researches, Duan et al. [13] once optimized the regenerative cooling structure based on a pseudo-density topology optimization model, and the optimized structure is further numerically tested in the thermal environment of engine's regenerative cooling system. It was found that the optimized structure can effectively reduce the average temperature. However, the optimized materials are water and aluminium, whose physical properties is quite different from that of hydrocarbon fuel, so whether the optimized structure could be used as a practical regenerative cooling channel remains to be further verified. Zhang et al. [14] conducted the topology optimization design for scramjet engine's regenerative cooling structure as well. It was observed that numerous micro-channels perpendicular to the main flow direction were generated in the optimized structure, which significantly improves the overall heat transfer performance. Nevertheless, the over-dispersed and perpendicular micro-channels lead to the formations of multiple backflow and stagnation zones, thereby resulting in multiple high-temperature regions.

It is found that the topology optimization of the engine's regenerative cooling structure remains an extremely challenging work. The main difficulty is that the flow and heat transfer in regenerative cooling channels is a complex fluid-thermal coupled problem, which involves turbulent flow with high Reynolds number, dramatic variation of the fuel's properties and compressible flow. Therefore, several improvement strategies are proposed in order to apply the topology optimization method to the engine's regenerative cooling structures. On one hand, a Brinkman-Forchheimer correction term was added to the momentum equation so that the fluid-solid boundary in the optimized layout is adaptively sharpened and an effective artificial resistance is formed within the flow field. Two penalty source terms were also respectively added into the k-ε turbulent equations. On the other hand, the variable physical properties of supercritical fluid were considered in TO model. The modified model was verified to be effective in the later topology optimization design and the conjugate heat transfer simulation.

The remain of this article is arranged as follows. In Section 2, the topology optimization model was firstly introduced, including the modified governing equations, optimization objective and constraints, and sensitivity analysis. In Section 3, a series of topology optimization designs for a multi-channel panel structure was conducted, and numerical investigate of flow and heat transfer performance of the conventional straight channel (SC) and the topology-optimized channel (TO) were researched. The final section is our conclusion.

2. Topology optimization model

2.1. Governing equations

The topology optimization design for a fluid-thermal coupled problem is schematized in Fig 1. The essence of the optimization is to find the optimal spatial distribution of fluid or solid material so as to satisfy the required objectives and constraints in the optimization model.

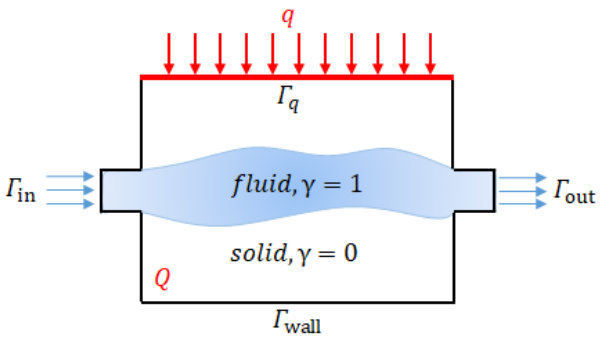

Fig 1. Schematic of the topology optimization design.

In conventional TO model, a viscous body force is added to the momentum equation compared with the steady-state Navier-Stokes equation, as listed in Eq. (1)-(2). The modified equation is known as Darcy-Brinkman equation, which is a classical flow model for porous media.

Navier-Stokes equation:

$$\nabla \cdot (\rho \boldsymbol{u}\boldsymbol{u}) = \nabla \cdot \boldsymbol{\tau} - \nabla p \tag{1}$$

Darcy-Brinkman equation:

$$\nabla \cdot (\rho \boldsymbol{u}\boldsymbol{u}) = \nabla \cdot \boldsymbol{\tau} - \nabla p - \alpha \boldsymbol{u} \tag{2}$$

where $\boldsymbol{u}$ and p respectively denotes the velocity and pressure. The viscous strain $\boldsymbol{\tau}$ is defined as $\boldsymbol{\tau} = 2\mu_{\text{eff}} S(\boldsymbol{u}) = \mu_{\text{eff}}(\nabla \boldsymbol{u} + \nabla \boldsymbol{u}^{\text{T}})$, μ_{eff} is the effective viscosity, α is generally interpolated by the following interpolation function [15,16]:

$$\alpha(\gamma) = \alpha_{\max} \frac{\theta(1-\gamma)}{\theta+\gamma} \tag{3}$$

where γ is the design variable (known as pseudo-density), and $\alpha_{\max}$ is generally a larger number that related to viscosity and inverse permeability. The additional term is utilized to provide effective artificial resistance when γ reaches 0. The shape of the interpolation function could be seen in Fig 2. Different from the homogeneous porous media, the permeability in the TO layouts are spatially changed due to the interpolation function.

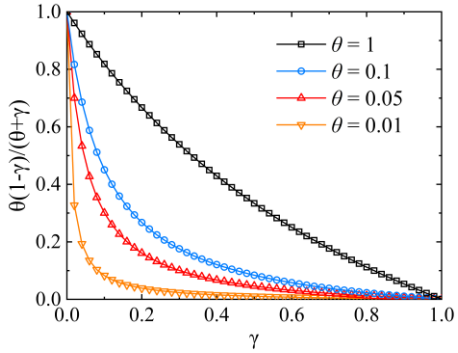

Fig 2. Interpolation function with different shape parameter θ

Apart from the momentum equation, the continuity and the energy equation are also included in the governing equations as follows:

$$\left(R_p, R_{\boldsymbol{u}}, R_T\right)^{\text{T}} = \begin{cases} -\nabla \cdot (\rho \boldsymbol{u}) \\ \nabla \cdot (\rho \boldsymbol{u}\boldsymbol{u}) - \nabla \cdot \boldsymbol{\tau} + \nabla p + \alpha(\gamma)\boldsymbol{u} \\ \nabla \cdot \left[\rho \boldsymbol{u}\left(h + \frac{1}{2}\boldsymbol{u} \cdot \boldsymbol{u}\right)\right] - \nabla \cdot \left[\left(\frac{\lambda(\gamma)}{C_p(\gamma)} + \frac{\mu_t}{Pr_t}\right)\nabla h\right] - \nabla \cdot (\boldsymbol{\tau} \cdot \boldsymbol{u}) - Q \end{cases} \tag{4}$$

where$\left(R_p, R_{\boldsymbol{u}}, R_T\right)^{\text{T}}$ denotes the equality constraint vector. The energy equation in the form of specific enthalpy is adopted, λ is the thermal conductivity, C_p is the specific heat at constant pressure, h is the specific enthalpy, and Q is the volumetric heat source. Similarly, the thermal conductivity and specific heat are interpolated in the following forms:

$$\lambda(\gamma) = \lambda_{\text{fluid}} + (\lambda_{\text{solid}} - \lambda_{\text{fluid}}) \frac{\theta(1-\gamma)}{\theta+\gamma} \tag{5}$$

$$C_p(\gamma) = C_{p\_\text{fluid}} + \left(C_{p\_\text{solid}} - C_{p\_\text{fluid}}\right) \frac{\theta(1-\gamma)}{\theta+\gamma} \tag{6}$$

The temperature could be further solved based on the following thermodynamic equation:

$$C_p = \left(\frac{\partial h}{\partial T}\right)_p \tag{7}$$

2.2. A boundary sharpening correction term

In the above pseudo-density based topology optimization model, the additional term in momentum equation is interpolated by pseudo-density γ. So that the flow is governed by Navier-Stokes equation when γ equals to 1, and the flow is governed by Darcy-Brinkman equation when γ equals to 0. With a relatively large number $\alpha_{\max}$, the additional term provides an artificial damping force and thus simulates the resistance between the fluid and solid domain in the porous media. To avoid the solid material from being permeated, the determination of $\alpha_{\max}$ is the most important task during the optimization procedure.

For most applications regarding to the topology optimization of flow and heat transfer problems [15-17], $\alpha_{\max}$ is defined as $\alpha_{\max} = \frac{\mu}{Da \cdot l^2}$, where Da is Darcy number and l is a characteristic scale. Olesen et al. [15] once suggested that it is more appropriate for Da to be less than or equal to 10^{-5}. Dilgen et al.[12] took Da as 10^{-6} in the topology optimization designs of turbulent flow. However, Yu et al. [16] found that when Da is equal to 10^{-5} or 10^{-6}, some wall-like structures are generated in the optimized configurations, which means that the solid areas are permeated and thus forming micro-channels. When Da is equal to 10^{-7}, this phenomenon can be avoided.

The above researches are working at different conditions, so it has to adjust Da number through trial and error. Moreover, it has to be noted that for flows in the porous media, the Darcy-Brinkman equation is only valid for low-speed laminar flow. As the Reynolds number increases, the inertia force becomes more significant than viscosity force [18]. To this end, Forchheimer once introduced the Forchheimer term to consider the effect of inertia force [19]. Alazmi and Vafai [20] proposed the combined Brinkman-Forchheimer correction term, which comprehensively considers all factors of viscous flow in the porous media and has been widely applied in the porous media's flow simulations.

Inspired by the above research, an artificial damping force incorporating both the viscous and inertial body forces is introduced in this paper, it refers to the Brinkman-Forchheimer modified Navier-Stokes equation in Ref.[21,22]. The modified momentum equation is rewritten as follows:

$$\nabla \cdot (\rho \boldsymbol{u}\boldsymbol{u}) = \nabla \cdot \boldsymbol{\tau} - \nabla p - [\alpha(\gamma) + \beta(\gamma)]\boldsymbol{u} \tag{8}$$

And the second term $\beta(\gamma)$ is formulated as:

$$\beta(\gamma) = \beta_{\max} \frac{\theta(1-\gamma)}{\theta+\gamma},\ \beta_{\max} = \frac{C_{\mathrm{f}}}{l\sqrt{Da}} \rho |\boldsymbol{u}| \tag{9}$$

where C_{f} is the drag coefficient in the porous media with a fixed porosity, $\beta_{\max}$ is the inertial force related coefficient. It is noted that with the modified model, $\beta(\gamma)$ equals to 0 when γ equals to 1, $|\boldsymbol{u}|$ equals to 0 and when γ equals to 0. So the additional term $-\beta(\gamma)\boldsymbol{u}$ mainly works on the gray regions between 0 and 1, and as the fluid-solid boundaries become clear during the optimization process, $-\beta(\gamma)\boldsymbol{u}$ will make a adaptively sharpening effect on the fluid-solid boundaries. In other words, it adaptively forms impermeable boundaries and protects the solid region from being permeated and split, therefore, it avoids forming unreasonable micro-channels in the optimized layouts to some extent. As for the turbulence model equation, a similar treatment as Ref.[23] is applied, i.e. two penalty source terms were respectively added into the *k-ε* turbulent equations.

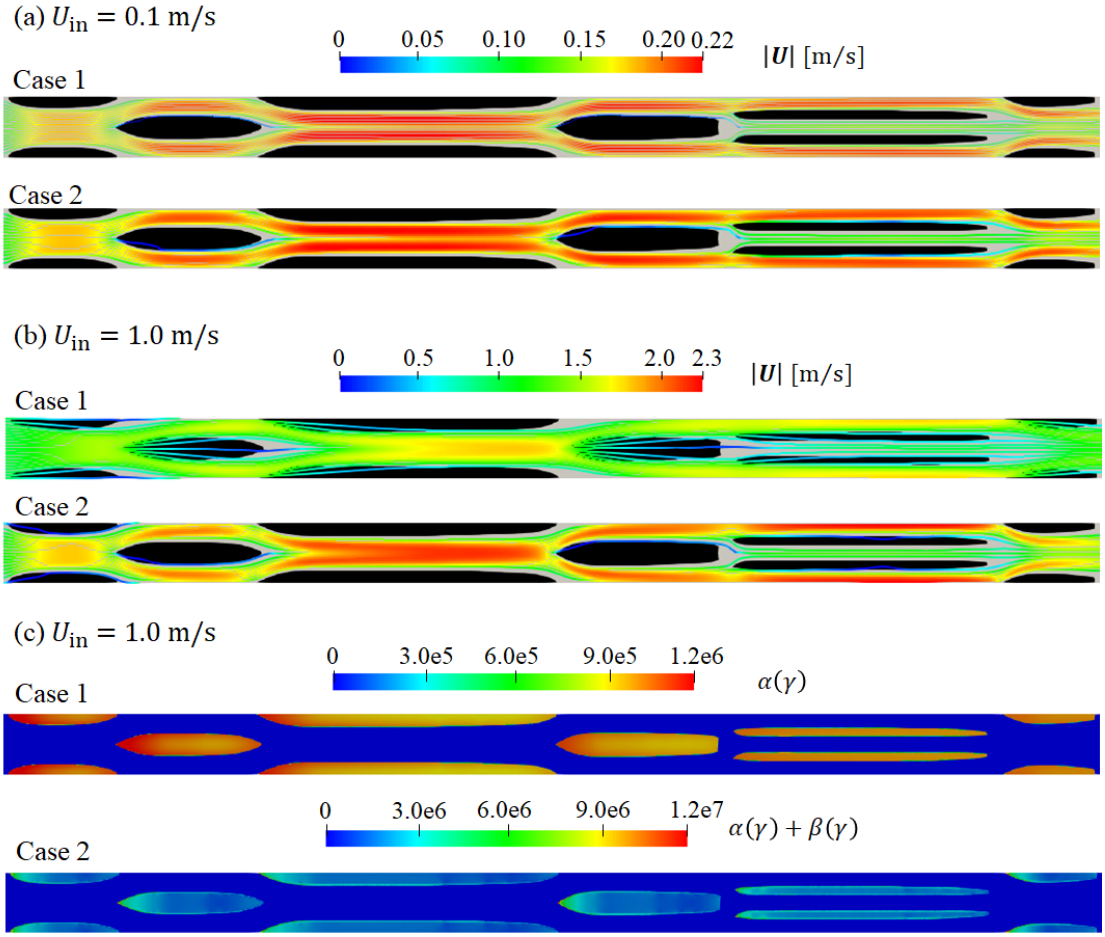

Fig 3. Comparion of the classical density-based topology optimization model and the modified model under different inlet Reynolds number (The black region represents the solid domain).

Taking the topology configuration in Fig 3 as an example, a comparison was made between the original topology optimization model (Case 1) and the modified model (Case 2). The velocity fields are

obtained by using the original model and the modified model, respectively ($Da = 10^{-4}$). It can be observed that under the low-speed laminar conditions, as shown in Fig 3(a), both Case 1 and Case 2 effectively resist the fluid around the solid regions, leading to flow separations in front of the solid cells. However, under the turbulent conditions in Fig 3(b), the solid regions in Case 1 are permeated with fluid, which implies that the resistance is weak to resist the fluid. As a contrast, the solid regions in Case 2 remains effective resistance to the fluid. Furthermore, in Fig 3(c), it demonstrates that the additional Forchheimer correction term sharps the fluid-solid boundaries and makes the solid regions impossible to permeate during the optimization process. Accordingly, the micro-channels or other unreasonable configurations are avoided in the final optimized layouts.

2.3. Mathematic formulation for TO model

As for objective function, a P-norm function is introduced as follows, aiming to reduce the maximum temperature of the design domain:

$$\Psi = \left(\int_\Omega T^m \mathrm{d}\Omega\right)^{\frac{1}{m}} \tag{10}$$

The value of m is set as 30. Then two inequality constraints, i.e. the power dissipation constraint and the volumetric fraction constraint, are adopted to avoid unreasonable configurations:

$$V_{\mathrm{fluid}} = \frac{1}{V}\int_\Omega \gamma \mathrm{d}\Omega \tag{11}$$

$$\varphi_{\mathrm{power}} = \int_\Gamma -\left(p + \frac{1}{2}\rho \boldsymbol{u}^2\right)\boldsymbol{u}\cdot\boldsymbol{n}\mathrm{d}\Gamma \tag{12}$$

$$\boldsymbol{G}(\boldsymbol{w},\gamma) = \left(g_{\mathrm{vol}}, g_{\mathrm{power}}, g_{\mathrm{uni}}\right)^T = \begin{cases} V_{\mathrm{fluid}} - V_{\max} \\ \varphi_{\mathrm{power}} - \varphi_{\max} \end{cases} \tag{13}$$

where V_{fluid} is the fluid material's volumetric fraction, φ_{power} is the power dissipation between the inlet and outlet of the fluid domain, $\boldsymbol{G}(\boldsymbol{w},\gamma)$ is the inequality constraint vector, $V_{\max}$ and $\varphi_{\max}$ are desired maximum constraint value of the two inequality constraints, respectively.

In summary, a complete topology optimization problem based on the pseudo-density method could be expressed as the following mathematical formulation:

$$\begin{cases} \text{Find:} & \gamma \\ \text{Minimize:} & \Psi(\boldsymbol{w},\gamma) \\ \text{Subject to:} & \boldsymbol{R}(\boldsymbol{w},\gamma) = 0 \\ & \boldsymbol{G}(\boldsymbol{w},\gamma) \le 0 \\ & 0 \le \gamma \le 1 \end{cases} \tag{14}$$

2.4. Sensitivity analysis based on continuous adjoint method

To solve the above TO problem, the sensitivity of objective w.r.t design variable should be computed. In this work, the sensitivity is derived based on the following continuous adjoint method. Firstly, a Lagrange function is constructed in the following form:

$$L = \Psi + \int_\Omega \boldsymbol{\lambda}\cdot\boldsymbol{R}(\boldsymbol{w},\gamma)\mathrm{d}\Omega = \Psi + \langle\boldsymbol{\lambda},\boldsymbol{R}(\boldsymbol{w},\gamma)\rangle \tag{15}$$

where $\boldsymbol{\lambda} = (p_a, \boldsymbol{u}_a, T_a)$ is Lagrange multiplier, also known as adjoint variable. Since that $\boldsymbol{R}(\boldsymbol{w},\gamma) = 0$, the sensitivity of objective function w.r.t design variable is equivalent to the total derivative of Lagrange function:

$$\frac{\mathrm{d}L}{\mathrm{d}\gamma} = \frac{\partial\Psi}{\partial\gamma} + \frac{\partial\Psi}{\partial\boldsymbol{w}}\frac{\mathrm{d}\boldsymbol{w}}{\mathrm{d}\gamma} + \frac{\partial\langle\boldsymbol{\lambda},\boldsymbol{R}\rangle}{\partial\gamma} + \frac{\partial\langle\boldsymbol{\lambda},\boldsymbol{R}\rangle}{\partial\boldsymbol{w}}\frac{\mathrm{d}\boldsymbol{w}}{\mathrm{d}\gamma} = \frac{\partial\Psi}{\partial\gamma} + \frac{\partial\langle\boldsymbol{\lambda},\boldsymbol{R}\rangle}{\partial\gamma} + \left(\frac{\partial\Psi}{\partial\boldsymbol{w}} + \frac{\partial\langle\boldsymbol{\lambda},\boldsymbol{R}\rangle}{\partial\boldsymbol{w}}\right)\frac{\mathrm{d}\boldsymbol{w}}{\mathrm{d}\gamma} \tag{16}$$

According to KKT (Karush-Kuhn-Tucker) conditions for the PDE constrained optimization [24], the equations of adjoint variables could be constructed as follows:

$$\frac{\partial\Psi}{\partial\boldsymbol{w}} + \frac{\partial\langle\boldsymbol{\lambda},\boldsymbol{R}\rangle}{\partial\boldsymbol{w}} = \begin{cases} \frac{\partial\Psi}{\partial p} + \frac{\partial\langle p_a,R_p\rangle}{\partial p} + \frac{\partial\langle\boldsymbol{u}_a,R_{\boldsymbol{u}}\rangle}{\partial p} + \frac{\partial\langle T_a,R_T\rangle}{\partial p} = 0 \\ \frac{\partial\Psi}{\partial\boldsymbol{u}} + \frac{\partial\langle p_a,R_p\rangle}{\partial\boldsymbol{u}} + \frac{\partial\langle\boldsymbol{u}_a,R_{\boldsymbol{u}}\rangle}{\partial\boldsymbol{u}} + \frac{\partial\langle T_a,R_T\rangle}{\partial\boldsymbol{u}} = 0 \\ \frac{\partial\Psi}{\partial T} + \frac{\partial\langle p_a,R_p\rangle}{\partial T} + \frac{\partial\langle\boldsymbol{u}_a,R_{\boldsymbol{u}}\rangle}{\partial T} + \frac{\partial\langle T_a,R_T\rangle}{\partial T} = 0 \end{cases} \tag{17}$$

At this point, the total derivative of Lagrange function, i.e. the sensitivity of the original objective function, is converted into the following form:

$$\frac{\mathrm{d}L}{\mathrm{d}\gamma} = \frac{\partial\Psi}{\partial\gamma} + \frac{\partial\langle\boldsymbol{\lambda},\boldsymbol{R}\rangle}{\partial\gamma} \tag{18}$$

After solving the state variable's and the adjoint variable's governing equations, the sensitivity could be computed. Then a gradient-based optimization algorithms MMA (the Method of Moving Asymptotes) is utilized as the optimizer to obtain the updated design variable γ, and the filter and projection strategies are employed at the end of the optimization process. Finally, a complete TO solver is constructed on

OpenFOAM, and the schematic of the topology optimization process is shown in Fig 4. It has to be noted that the adjoint variables $(p_b, \boldsymbol{u}_b)$ are served for the inequality constraint function of flow power dissipation, whose derivation of sensitivity is not presented here.

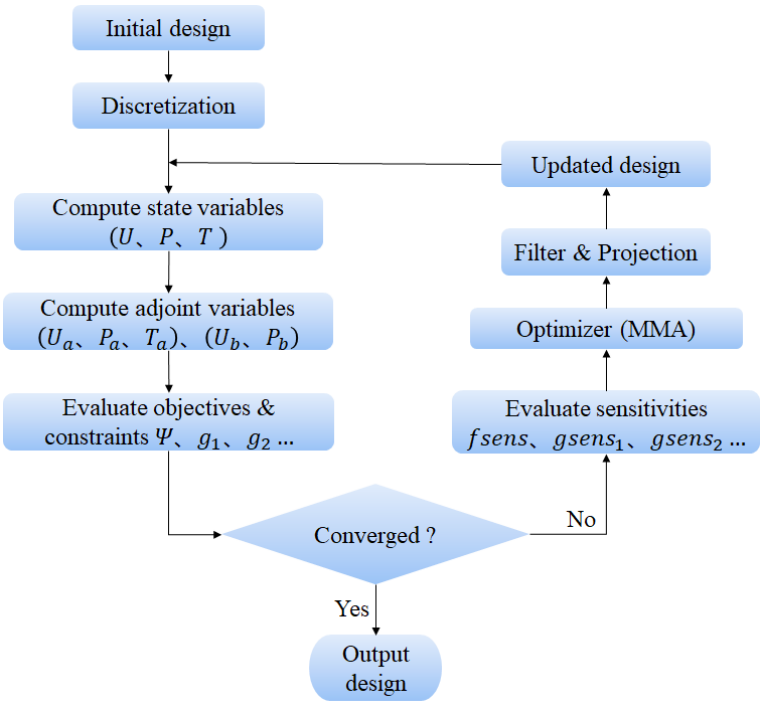

Fig 4. Schematic of the topology optimization process.

3. Results and discussion

3.1. Topology optimization results

A schematic of geometry layout and boundary conditions of the design domain is presented in Fig 5(a). The size parameter d of the design domain is 5 mm, and the thickness is 2 mm. The middle section constitutes the design domain, while the regions colored in blue are non-design domains, i.e. the pure fluid regions. The coolant is n-decane, which is a typical one-component substitute for kerosene, and the solid material is GH3128. To facilitate the generation of cooling channels in such large-area design domain, a non-uniform layout, as depicted in Fig 5(b), is initialized to complete the optimization design.

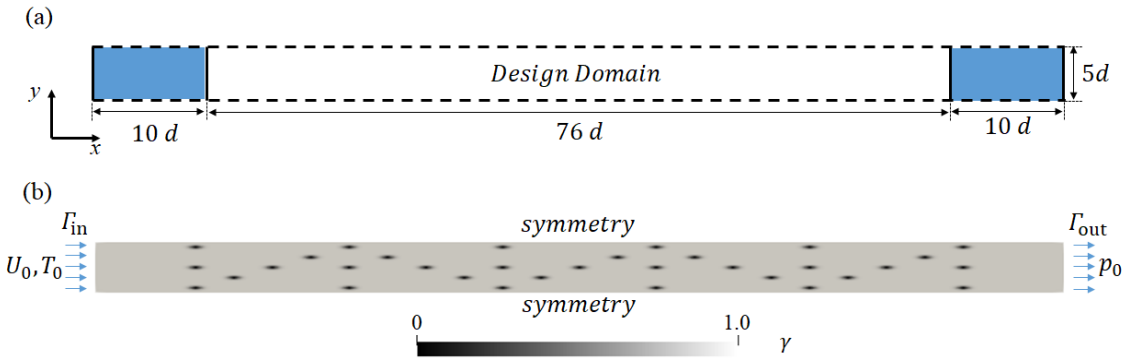

Fig 5. (a) Geometry size (b) Initial and boundary conditions.

The computational conditions are listed as follows. The inlet's mass flow rate is set to 0.018 kg/s, the inlet's coolant temperature is 600 K, which corresponds to an approximate inlet Reynolds number 18690. The outlet's pressure is set to 3 MPa. An uniform volumetric heat source $Q = 5 \times 10^8\ \mathrm{W/m^3}$ is loaded on the design domain. The computational domain is discretized by uniform structured grids with a grid size of 0.2 mm × 0.2 mm, and the total grids number is 300000.

To investigate the influence of different power dissipation constraint values on the topology optimization configurations, the flow field of the initial distribution configuration is firstly computed. The power dissipation value between inlet and outlet is about 0.078 $\mathrm{kg}\cdot\mathrm{m/s^2}$. Subsequently, a series of optimization cases with power dissipation values of $\varphi_{\max}$ from 0.20 to 0.40 are conducted. The desired volumetric fraction is set to 0.68. The Darcy number Da is set to 10^{-6}. In these cases, five configurations with $\varphi_{\max}$ values of 0.25, 0.28, 0.31, 0.34, and 0.35 are respectively extracted and named as Case 1 to Case 5.

Fig 6 depicts the five optimized configurations of Case 1 to Case 5. Fig 6 and Fig 7 show the corresponding temperature and velocity field, respectively. It can be seen that from Case 1 to Case 5, the number of the split solid cells increases gradually, so the topology configurations become more and more complicated, it naturally results in more flow separation and remixing of the fluid. In Case 1, the structure is primarily composed of elongated solid cells that arranged in parallel, whereas in Case 5, the structure is mainly composed of short and stout solid cells that arranged in a staggered manner, it also generates wavy boundaries in some long solid cells. As for the temperature field, there are two high-temperature regions are generated in Case 1 (i.e. 100~150 mm, 350~430 mm), while in Case 5, the solid blocks near the two high-temperature regions are split, which leads to flow separation of the coolant and thus decreases the temperature. Additionally, with the increase of power dissipation, the average velocity in fives channel increases as well.

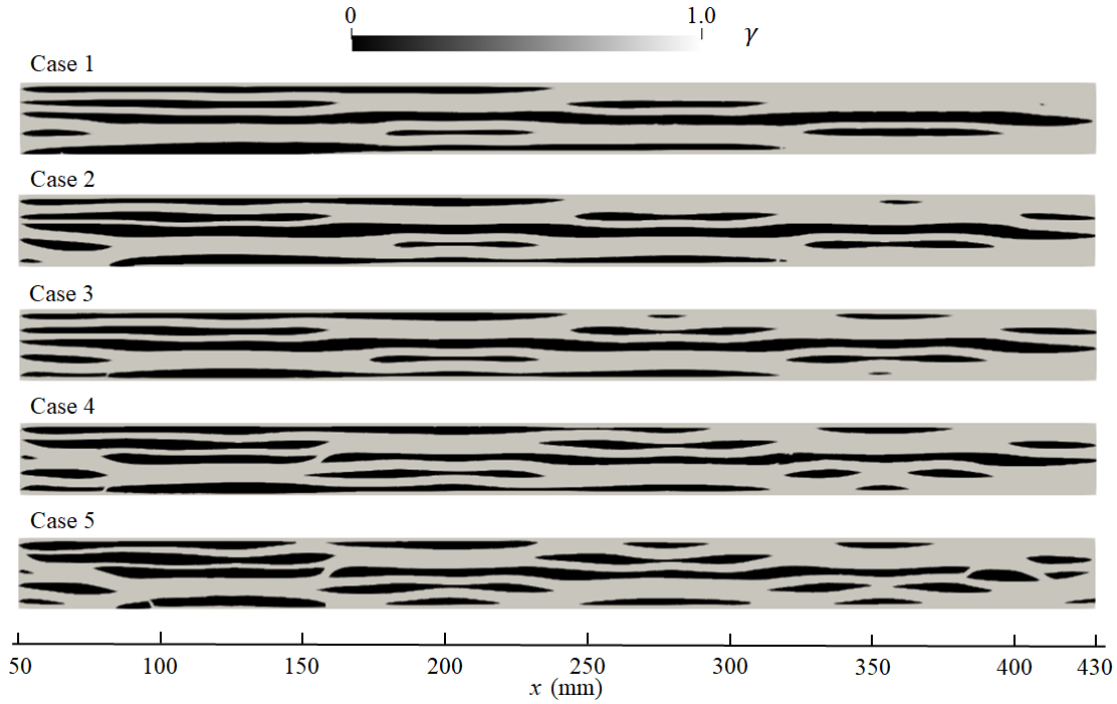

Fig 6. Optimized layouts of Case 1 to Case 5. (The black area is solid material, the gray area is fluid material).

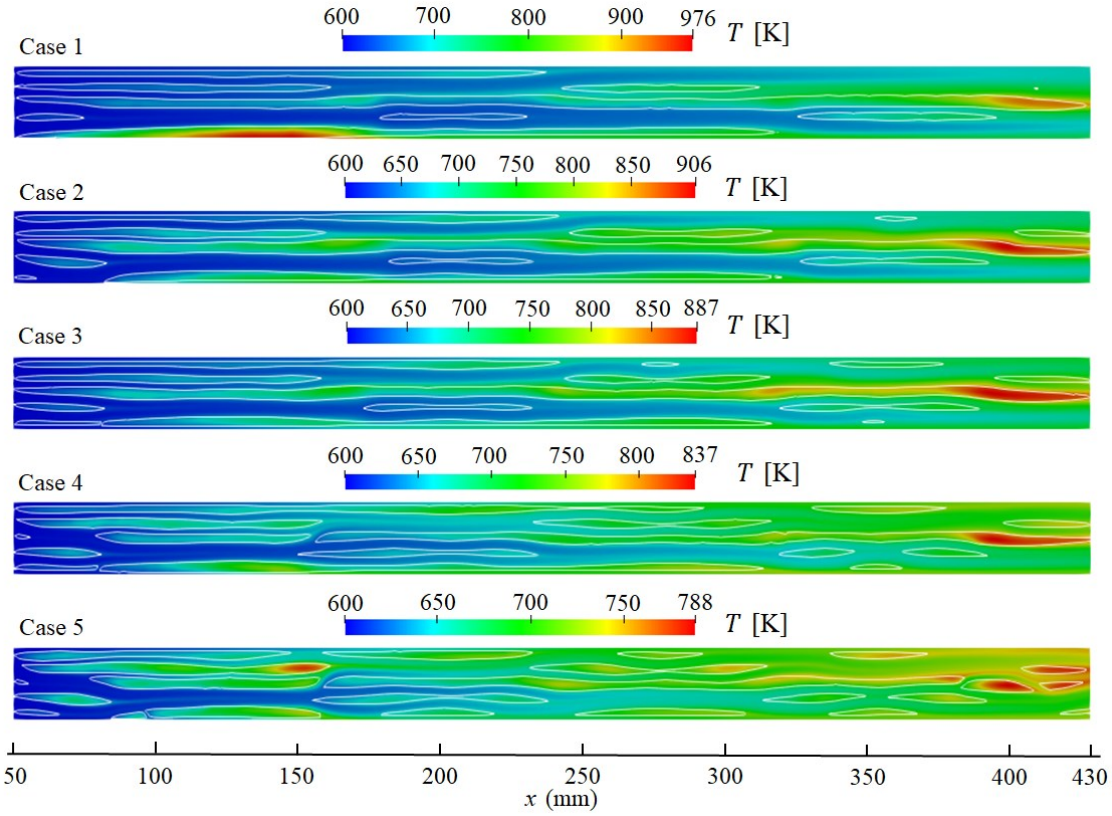

Fig 7. Contours of temperature fields of Case 1 to Case 5.

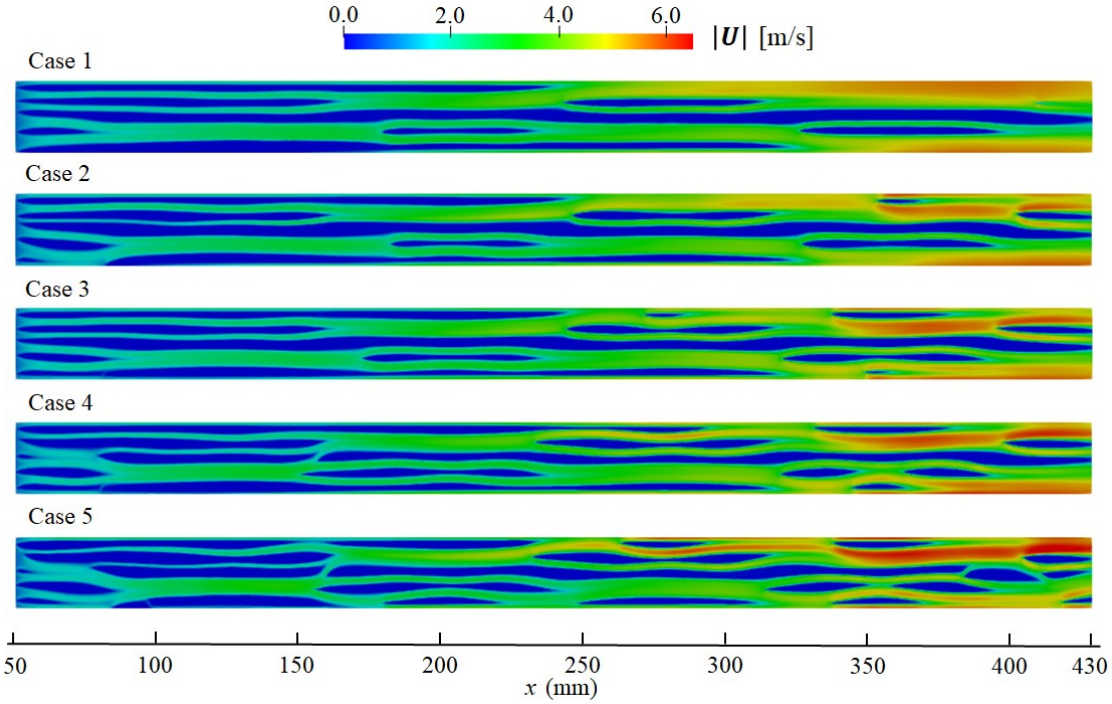

Fig 8. Contours of velocity fields of Case 1 to Case 5.

3.2. Conjugate heat transfer simulation

To further investigate the flow and heat transfer performance of the topology optimized structure, the optimized configuration of Case 5 will be extracted, and the conjugate heat transfer of the three-dimensional structure will be numerically simulated in this section. A conventional straight channel is

introduced as a comparison, the width and height of the solid ribs is respectively 4.33 mm and 2 mm, and the thickness of the upper and lower base layers are 0.75 mm. The straight channel and the topology optimized channel are respectively referred to as SC and TO.

Fig 9 clearly presents the cells structure in the middle layers of two channels. Through comparison, the ration of the solid volume of TO channel to that of SC channel is approximately 84.7%, which implies that the weight of channel TO reduces by 15.3%. The computational conditions are set as follows: the inlet's mass flow rate is 0.018 kg/s, the inlet temperature of coolant is 600 K, and the outlet pressure is set to 3 MPa, which are consistent with the conditions in optimization process. According to the principle of energy conservation, the volume heat source Q is converted into a surface heat flux q that imposed on the bottom surface of the solid domain, and the magnitude of the heat flux is 1 MW/m^2. The left and right surfaces of the whole domain are set to symmetric conditions.

The computational domain is discretized by unstructured polyhedral grids, and the prism grids are generated near the coupled surfaces in fluid domain. The grid height of the first boundary layer is 2 μm to ensure that dimensionless distance $y^+<5$, and the grids near the leading and trailing edges of the solid cells are refined. Three sets of grids are generated by adjusting the maximum grid size of the fluid domain. According to the mesh independence verification, the final number of grids for channel SC and TO is 622w and 660w, respectively. Fig 10 presents the mesh details of channel TO. The SST k-ω turbulence model is then utilized for simulation.

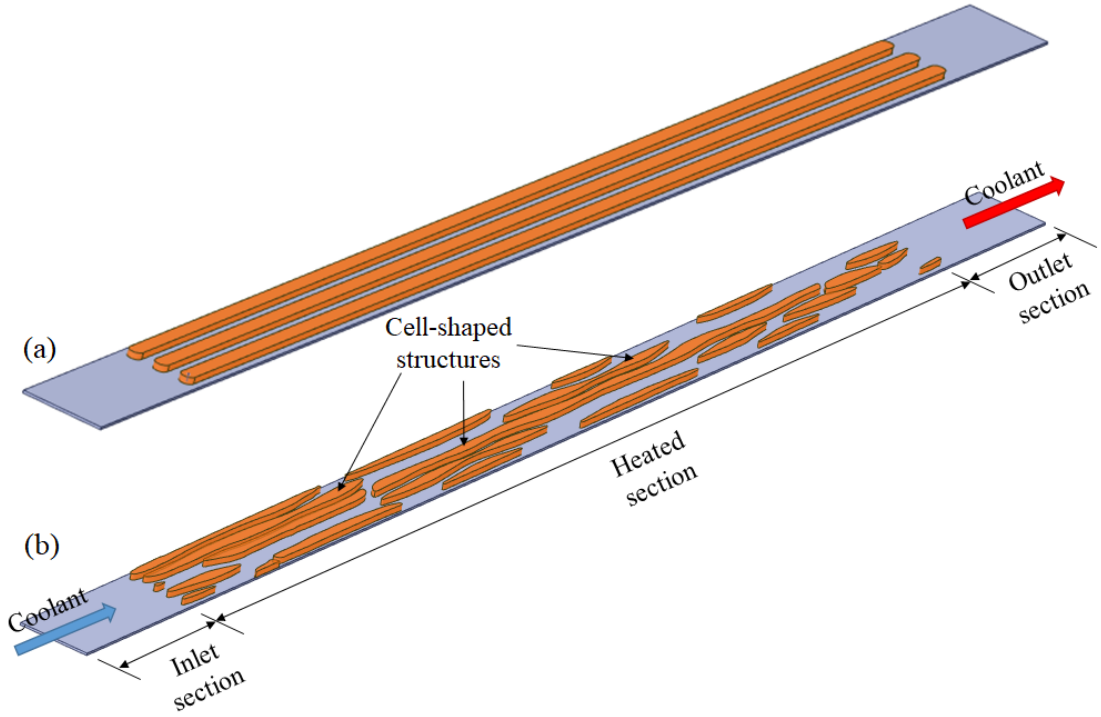

Fig 9. Schematic of the cell-shaped structures of channel SC and TO.

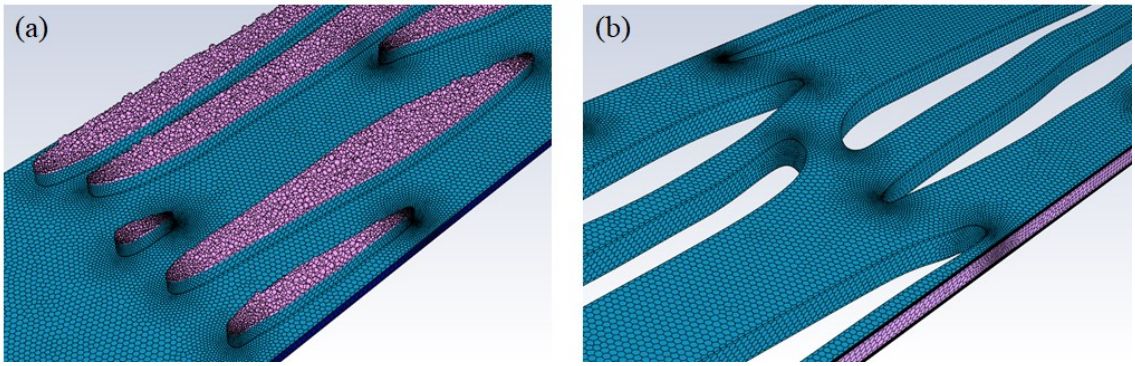

Fig 10. The computational mesh of channel TO (a) local mesh of solid domain (b) local mesh of fluid domain.

Fig 11 illustrates the contours of velocity, pressure, and turbulent kinetic energy on the central plane of the fluid domain. Due to the smaller solid volume fraction of channel TO, its average flow cross-sectional area is larger and its average velocity is significantly lower than that in channel SC. When the coolant flow through the solid cells, it obviously causes localized pressure drop losses and power dissipation, however, the lower average velocity in channel TO results in smaller total pressure drop compared to channel SC. Furthermore, the staggered arrangement of solid cells in channel TO leads to multiple flow separations and re-mixing of the coolant, the flow boundary layers are break and reattached on solid cells periodically, which significantly reduce the thermal resistance and enhance the local heat transfer performance. Additionally, the turbulent kinetic energy is motivated at multiple leading and trailing edges of solid cells and curved boundaries, such as the positions along the flow direction at $x = 160\text{mm}$, $x = 310\text{mm}$, and $x = 390\text{mm}$, which also demonstrates that the heat transfer between coolant and hot walls are enhanced.

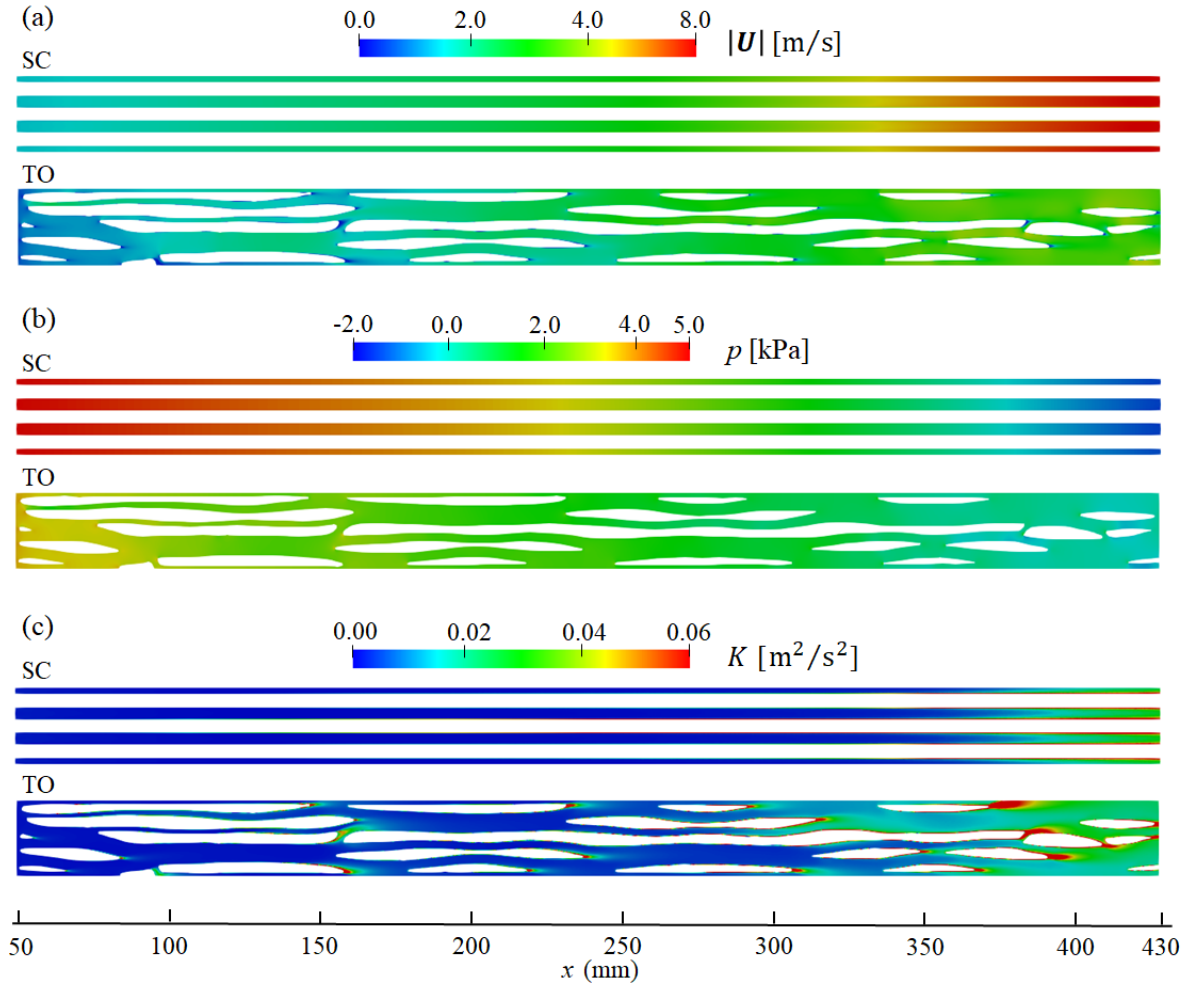

Fig 11. Contours of velocity, pressure and turbulent kinetic energy fields of channel SC and TO.

Fig 12 presents the distribution of temperature on central plane and heated wall's surface. It clearly shows that a large area of high-temperature is generated in the front part ($x = 100\sim250\text{mm}$) of channel SC, but its axial wall temperature gradually decreases along the flow direction. The main reason for this change is that when the coolant flows in, the coolant's initial temperature is significantly lower than the wall's temperature, so the thermal acceleration effect leads to significant heat transfer deterioration, but when the coolant temperature surpasses its pseudo-critical temperature, the phenomenon of heat transfer deterioration will be gradually eliminated. As a contrast, the high-temperature regions in channel TO is significantly reduced than that in SC. On one hand, the high-temperature regions are mainly located around the solid cells' gaps with larger transverse spacing, where the coolant velocity is relatively slow. On the other hand, the low-temperature regions are mainly located at the leading edges of solid cells, curved boundaries and positions with higher local velocities,

it exactly corresponds to the locations where turbulent kinetic energy is significantly stimulated. It indicates that the heat transfer is locally enhanced at these positions and the heat transfer deterioration is thus weakened.

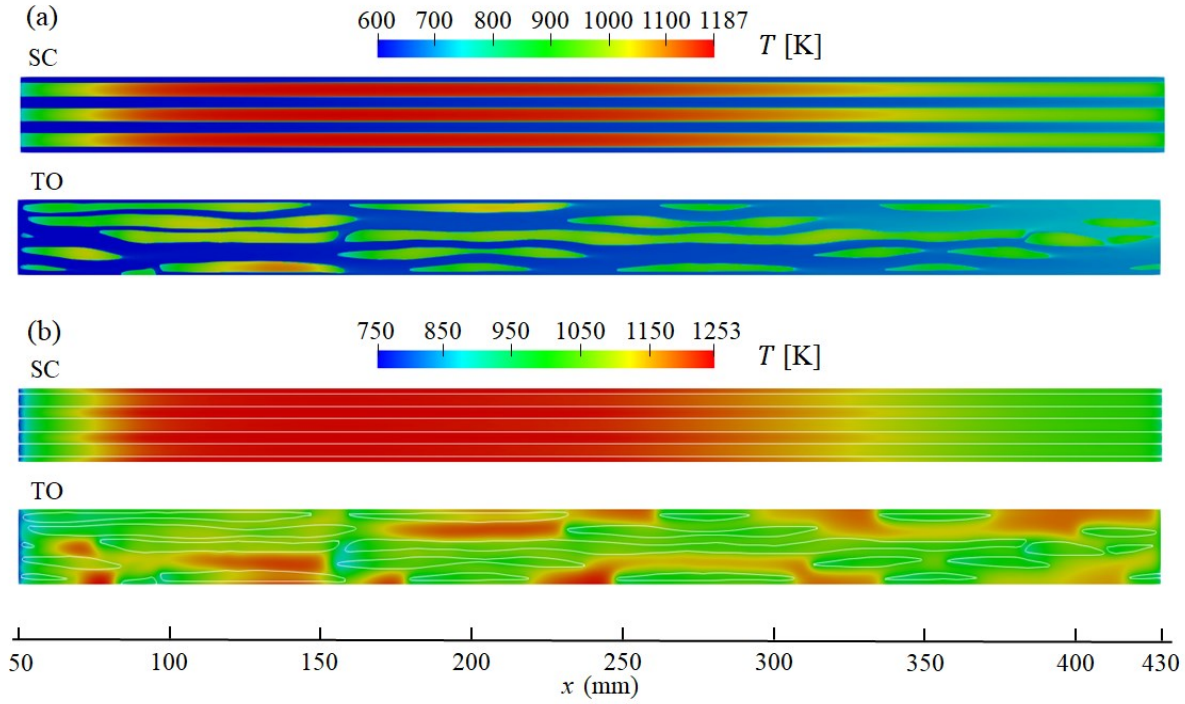

Fig 12. Contours of temperature fields on the central plane and the heated wall's surface.

The Q criterion is employed to recognize vortex structures in the fluid domain. Fig 13 presents the isosurface of $Q = 10^5$ s^{-1}, which is colored by velocity magnitude. It shows that in channel SC, vortex structures are generated near the leading and trailing edges, but only small-scale and fragmented vortices are existed in the internal fluid domain. In contrast, vortex structures are generated at the leading and trailing edges of each split solid cells in channel TO, and attached vortex structures are formed on the sidewall's surfaces where the surface curvature changes remarkably. Subsequently, these attached vortex structures gradually dissipate into small-scale vortices due to viscous stress force. Until the fluid flows through the next split solid cell, large-scale vortex structures are regenerated again. It demonstrates that the separated and curved flow of coolant motivate the generation of vortex structures in channel TO, enhancing the remixing and heat transfer between the coolant and the heated wall, and finally reducing the temperature of the heated wall's surface.

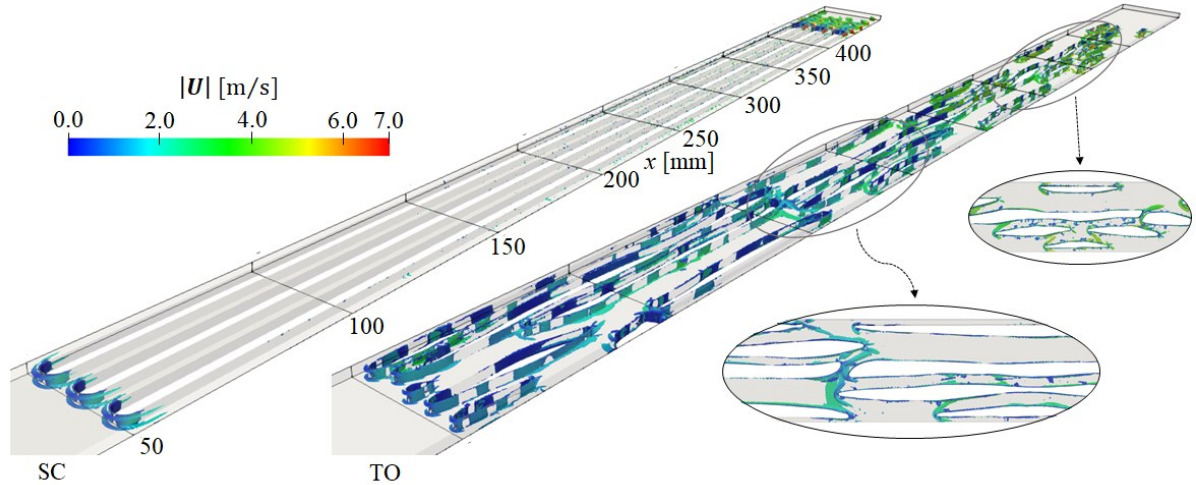

Fig 13. Contours of vorticity of channel SC and TO (Q = 10^5 s^{-1}).

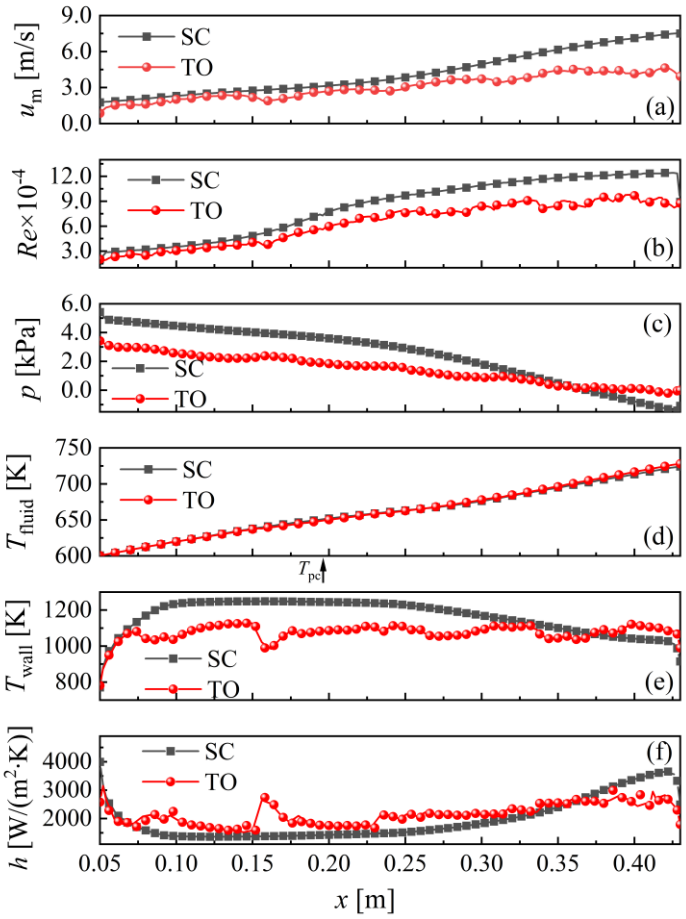

Fig 14. Comparison of the performance along the x-direction of channel SC and TO (a)average temperature (b)local Reynolds number (c)relative pressure (d)coolant bulk temperature (e)average temperature of the heated surface (f)heat transfer coefficient.

Fig 14 gives the distribution of coolant velocity, local Reynolds number, relative pressure, bulk temperature, average temperature of the heated surface, and heat transfer coefficient along the *x*-axis. It can be observed that the coolant velocity and Reynolds number in channel TO channel are consistently smaller than those in channel SC. The difference between them are gradually increases after the coolant reaches its pseudo-critical temperature($x = 195\text{mm}, T_{\text{pc}} = 648.5\text{K}$). It mainly because that in the latter section of channel TO, the proportion of solid areas decreases and the spacing between the solid cells become obviously larger, so it results in that the average hydraulic diameter is larger but the average velocity is lower than that in channel SC.

After surpassing the pseudo-critical temperature, the heat transfer coefficient in SC channel gradually increases. It indicates that the heat acceleration effect is gradually vanished, and it changes from heat transfer deterioration to heat transfer enhancement. Consequently, the average temperature on the heated wall gradually decreases. In contrast, the heat transfer coefficient of channel TO is consistently greater than that of channel SC within the range of $x = 70\sim370\text{mm}$. However, the heat transfer coefficient of channel TO becomes lower than that of channel SC at the positions $x > 370\text{mm}$, and the temperature of the heated wall gradually exceeds that of channel SC. It is noteworthy that there a distinct heat transfer enhancement from $x = 150\sim170\ mm$ in channel TO, which is attributed to the complex flow state of coolant at this position. The local vortex structure diagram in Fig 13 confirms this viewpoint. The above comparisons indicate that the unique configuration of the TO channel significantly alleviates the heat transfer deterioration phenomenon before the coolant reaches its pseudo-critical point. However, for regions where the coolant exceeds its pseudo-critical point, the heat transfer performance of TO channel is inferior to that of SC channel.

Table 1 presents a comparative data of the flow and heat transfer performance of two channels. The outlet temperature of the coolant in channel TO is 3.7 K higher than that in SC, which is relatively

close. Compared to channel SC, the maximum temperature on the heated wall of channel TO only decreases by 10.7 K, while its average temperature decreases by 89.9 K, corresponding to a reduction of 7.7%. Additionally, the pressure drop from the inlet to outlet of channel TO decreases by 2.9 kPa, corresponding to a reduction of 45.3%. As for the overall performance, the average Nusselt number of channel TO is 1.322 times that of channel SC, while the resistance coefficient is 1.207 times that of channel SC. The overall thermal performance factor is 1.243, which indicates that under the same pump power cost, the heat transfer efficiency of channel TO improves by 24.3% than channel SC.

Table 1. Flow and heat transfer performances of channel SC and TO

	T_{out} [K]	T_{max} [K]	T_{ave} [K]	Δp [kPa]	Nu	f	η
SC	724.2	1252.6	1163.9	6.4	76.3	0.029	\
TO	727.9	1241.9	1074.0	3.5	100.9	0.035	1.243

4. Conclusions

This paper focuses on the topology optimization design of engine's regenerative cooling structures, the main conclusions are summarized as follows:

(1) A modified topology optimization model is addressed to solve the topology optimization of high Reynolds number flow problem. An artificial damping force that related to Reynolds number is introduced into the momentum equation, which compensates for the shortcomings of classical topology optimization models in simulating high Reynolds number flows in the porous media. The strategies are verified to be effective for the topology optimization of fluid-thermal coupled problem with high Reynolds number and variable physical properties.

(2) Through the fluid-thermal coupled topology optimization design of multi-channel design domains, it was observed that the topology optimization configurations become increasingly complex with the increase of power dissipation constraint values. Additionally, the flow separation and re-mixing of the coolant are verified to be effective to reduce the high-temperature regions.

(3) Through the numerical simulations of conjugate heat transfer for the straight channel (SC) and the topology optimization channel (TO), it was found that in channel TO, the staggered arrangement of cells in channel TO leads to multiple flow separation and re-mixing of the coolant. It helps to generate complex vortex structures and motivate the turbulent kinetic energy, enhancing the local heat transfer performance and resulting in superior overall heat transfer performance. It indicates that the weight of channel TO reduces by 15.3%, but the overall thermal performance of channel TO improves by 24.3% than that of channel SC.

To sum up, the topology optimization cooling structures present superior flow and heat transfer performance, making it a promising tool for engineering applications.

References

1. Boeing Company, Boeing X-51A WaveRider Sets Record with Successful 4th Flight, Boeing Company Press Release, 2013 https://boeing.mediaroom.com/2013-05-03-Boeing-X-51A-WaveRider-Sets-Record-with-Successful-4th-Flight.
2. Li Y, Xie G, Sunden B. Flow and thermal performance of supercritical n-Decane in double-layer channels for regenerative cooling of a scramjet combustor[J]. Applied Thermal Engineering, 2020, 180: 115695.
3. Sunden B A, Wu Z, Huang D. Comparison of heat transfer characteristics of aviation kerosene flowing in smooth and enhanced mini tubes at supercritical pressures[J]. International Journal of Numerical Methods for Heat & Fluid Flow, 2016, 26(3/4): 1289-1308.
4. Li X, Lu Y, Wu K, et al. A Novel Method of Cooling Channel Optimization for Active-Cooled Structure Using the Calculus of Variations[C]. AIAA Propulsion and Energy 2019 Forum. 2019.
5. Li X, Zhang S, Qin J, et al. Parametric analysis on the thermal behavior of cracking hydrocarbon fuel flow inside asymmetry heated cooling channels with micro-ribs[J]. International Journal of Heat and Mass Transfer, 2020, 160: 120154.
6. Li N, Huang Z, Bu Y, et al. Effects of channel geometries and acceleration on heat transfer of hydrocarbon fuel[J]. Journal of Thermophysics and Heat Transfer, 2020, 34(3): 570-578.

7. Fawaz A, Hua Y, Corre S L, et al. Topology optimization of heat exchangers: A review[J]. Energy, 2022, 252: 124053.
8. Borrvall T, Petersson J. Topology optimization of fluids in Stokes flow[J]. International journal for numerical methods in fluids, 2003, 41(1): 77-107.
9. Gersborg-Hansen A, Sigmund O, Haber R B. Topology optimization of channel flow problems[J]. Structural and multidisciplinary optimization, 2005, 30(3): 181-192.
10. Othmer C. A continuous adjoint formulation for the computation of topological and surface sensitivities of ducted flows[J]. International Journal for Numerical Methods in Fluids. 2008, 58(8): 861-877.
11. Yoon G H. Topology optimization for turbulent flow with Spalart–Allmaras model[J]. Computer Methods in Applied Mechanics and Engineering, 2016, 303: 288-311.
12. Dilgen S B, Dilgen C B, Fuhrman D R, et al. Density based topology optimization of turbulent flow heat transfer systems[J]. Structural and Multidisciplinary Optimization, 2018, 57: 1905-1918.
13. Duan Z, Xie G, Li X. Topology Optimization Design of Scramjet Structures with Forced Convective Heat Transfer on Unstructured Meshes[J]. Journal of Thermal Science and Engineering Applications, 2023, 15(1): 011011.
14. Zhang T, Jing T, Qin F, et al. Topology optimization of regenerative cooling channel in non-uniform thermal environment of hypersonic engine[J]. Applied Thermal Engineering, 2023, 219: 119384.
15. Olesen L H, Okkels F, Bruus H. A high-level programming-language implementation of topology optimization applied to steady-state Navier–Stokes flow[J]. International Journal for Numerical Methods in Engineering, 2010, 65(7): 975-1001.
16. Yu M, Ruan S, Gu J, et al. Three-dimensional topology optimization of thermal-fluid-structural problems for cooling system design[J]. Structural and Multidisciplinary Optimization, 2020, 62(6): 3347-3366.
17. Xia Y, Chen L, Luo J, et al. Numerical investigation of microchannel heat sinks with different inlets and outlets based on topology optimization[J]. Applied Energy, 2023, 330: 120335.
18. Eisfeld B, Schnitzlein K. The influence of confining walls on the pressure drop in packed beds[J]. Chemical Engineering Science, 2001, 56(14): 4321-4329.
19. Forchheimer P. Wasserbewegung durch Boden[J]. Zeits. Ver. Deutsch. Ing., 1901, 45: 1782-1788.
20. Alazmi B, Vafai K. Analysis of variants within the porous media transport models[J]. Journal of Heat Transfer, 2000, 122(2): 303-326.
21. Whitaker S. The Forchheimer equation: a theoretical development[J]. Transport Porous Media, 1996, 25: 27–61.
22. Wood B D, He X, Apte S V. Modeling turbulent flows in porous media[J]. Annual Review of Fluid Mechanics, 2020, 52: 171-203.
23. Yoon G H. Topology optimization method with finite elements based on the k-ε turbulence model[J]. Computer Methods in Applied Mechanics and Engineering, 2020, 361: 112784.
24. Hinze M, Pinnau R, Ulbrich M, and Ulbrich S. Optimization with PDE Constraints[M]. Springer, 2009.